Geomorphology 235 (2015) 106–117

Contents lists available at ScienceDirect

Geomorphology

journal homepage: www.elsevier.com/locate/geomorph

High-precision levelling, DInSAR and geomorphological effects in the Emilia 2012 epicentral area

R. Caputo [a,b,*], A. Pellegrinelli [c], C. Bignami [d], A. Bondesan [e], A. Mantovani [a], S. Stramondo [d], P. Russo [c]

[a] Dept. of Physics and Earth Sciences, University of Ferrara, Italy
[b] Research and Teaching Centre for Earthquake Geology, Tyrnavos, Greece
[c] Dept. of Engineering, University of Ferrara, Italy
[d] Istituto Nazionale di Geofisica e Vulcanologia, Rome, Italy
[e] Consorzio di Bonifica Pianura di Ferrara, Ferrara, Italy

ARTICLE INFO

Article history:
Received 30 May 2014
Received in revised form 6 February 2015
Accepted 7 February 2015
Available online 14 February 2015

Keywords:
Co-seismic deformation
DInSAR
Levelling
Site effects
Po Plain

ABSTRACT

In May 2012, two moderate earthquakes (M_w = 6.1 and 5.9), associated with a noticeable aftershock sequence affected the eastern sector of the Po Plain, northern Italy. The co-seismic areal uplift events are crucial for a better understanding of the seismotectonics of the broader area and thus for a better assessment of the seismic hazard in the region. In the present study, we compared the results of analyses based on high precision levelling, the DInSAR technique, the distribution of liquefaction occurrences, the geomorphological map of the area and the structural model of the region. The DInSAR technique revealed a marked uplift of the ground (up to 17 cm), which was confirmed by high precision levelling. The results of both techniques substantially agreed, although there were some considerable local discrepancies, due to well-documented and diffuse liquefaction phenomena. Some strategic precautions when planning high-precision levelling networks are suggested.

1. Introduction

In May 2012, two moderate (M_w = 6.1 and 5.9; *e.g.* Pondrelli et al., 2012) earthquakes, associated with a noticeable aftershock sequence (*e.g.* Saraò and Peruzza, 2012; Scognamiglio et al., 2012), affected the eastern sector of the Po Plain, Italy (Fig. 1). The causative faults are two segments of the Ferrara Arc thrust system representing the front most portion of the buried Northern Apennines fold-and-thrust belt (Fig. 1). In particular, the two major structures that were reactivated have a left-stepping largely overlapping geometry. Both seismogenic sources were associated with blind, mainly dip-slip reverse, faulting (*e.g.* Pondrelli et al., 2012; Scognamiglio et al., 2012), while the uppermost tip segment of the sliding planes has been estimated to reach a minimum depth of 3–4 km (Bignami et al., 2012). As a consequence of the fault geometry and kinematics, the rock volume above the co-seismic rupture tip was characterized by a typical fault-propagation folding process that eventually caused the bending of the topographic surface and the consequent uplift of the broader epicentral area (Bignami et al., 2012; Salvi et al., 2012).

Notwithstanding the high sedimentation rate characterizing the Po Plain, the recurrence of similar 'areal morphogenic earthquakes' (Caputo, 2005) during the Late Pleistocene and Holocene has caused cumulative effects on the local coeval stratigraphic succession, but also on the present-day morphology of the region. Although such lateral stratigraphic variations are fairly evident in the deeper geology (*e.g.* Pieri and Groppi, 1981), they are morphologically subtle in the otherwise flat topography of the alluvial plain (Fig. 1) and can only be detected by careful inspection of the hydrographic network, which however highlights the occurrence of several drainage anomalies (*e.g.* Burrato et al., 2003, 2012). Indeed, these hydrographic anomalies were considered key features for documenting the recent tectonic activity of buried faults (Basili et al., 2008; DISS WG, 2010) whose instrumental seismic record is generally poor, likely due to the long recurrence intervals.

These co-seismic areal uplift events are crucial for a better understanding of the seismotectonics of the broader area and thus for a better assessment of the seismic hazard in the region. Therefore, the principal aims of the present study were i) to analyse in detail the available geodetic information concerning the May 2012 Emilia earthquakes for improving our knowledge about the active tectonics of the region, ii) to compare the results of two different techniques, namely high-precision levelling (HPL) and Differential Synthetic Aperture Radar interferometry (DInSAR; Massonnet et al., 1993), iii) to determine their pros and cons and the possible complementarity of the two methods, and iv) to discuss the consequences of site effects induced by liquefaction phenomena in terms of the vertical motion detected by the two geodetic methods. We briefly outline the principles of the two approaches and then, compare the independently obtained results.

* Corresponding author at: Dept. of Physics and Earth Sciences, University of Ferrara, Italy. Tel.: +39 0532 974688.
E-mail address: rcaputo@unife.it (R. Caputo).

http://dx.doi.org/10.1016/j.geomorph.2015.02.002
0169-555X/

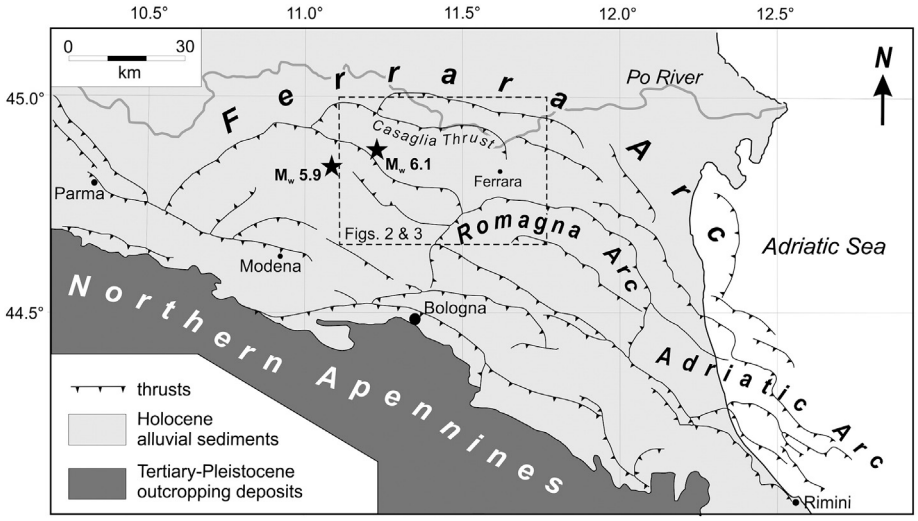

Fig. 1. Tectonic framework of northern Italy, showing the buried Northern Apennines fold-and-thrust belt underlying the Po Plain and the major tectonic structures (modified from Bigi et al., 1990). Stars indicate the epicenters of the two principal earthquakes of the May–June 2012 seismic sequence (May 20, $M_L = 5.9$ and May 29, $M_L = 5.8$). The box indicates the location of Figs. 2 and 3.

Finally, we analyse in detail how the occurrence of seismologically induced site effects could affect the geodetic measurements and we suggest some strategic precautions when planning an HPL network.

2. Hydrographic and morphological evolution of the western Ferrara Plain

The back-bone of the Italian Peninsula is represented by the Apennines, a 1000 km-long mountain chain developed in the framework of the mainly Tertiary Africa–Europe convergence. In particular, the Neogene fold-and-thrust belt largely outcrops in the reliefs of the Northern Apennines. NNE–SSW convergence continued during the Quaternary, causing thrusts to propagate further northwards (Fig. 1). However, the coeval set-up of strong regional subsidence combined with the high deposition rates characterizing the Po Plain foredeep entirely buried the growing tectonic structures by continuously blanketing them and levelling any differential vertical movement induced by faulting and folding.

Only indirect information, such as seismic profiles, oil wells and gravimetric surveys, allows us to reconstruct the articulated geometry of the major tectonic structures underlying this morphologically flat area (Fig. 1; *e.g.* Bigi et al., 1990). All recognized faults are clearly blind and their Pleistocene and Holocene seismogenic activity is inferred solely from the very gentle folding of the sedimentary units overlying the fault tips. Indeed, beyond the 2012 seismic sequence, only a few historical events have been attributed with some confidence to specific seismogenic sources (Basili et al., 2008) and the long recurrence intervals certainly do not help in this regard.

In the framework of this tectonic evolution, the present-day morphology of the western Ferrara Plain, corresponding to the central sector of the Ferrara Arc (Fig. 1), is the direct result of competition among high deposition rates, tectonic activity and differential compaction, as well as the latest Pleistocene–Holocene climatic variations. These natural phenomena basically caused differential vertical movements which governed the recent hydrographic evolution and caused a highly variable (both lateral and vertical) sedimentary distribution in the shallow subsoil. As a consequence, the alluvial plain was crossed by only a few watercourses at any one time, although at present it is characterized by many abandoned river channels and widespread flood deposits (Fig. 2). All these sedimentary bodies generally represent distinct morphological features that stand out altimetrically from the otherwise flat territory. Their topographic evidence (up to several meters) is commonly proportional to the importance of the channel and to their age. However, in the last two millennia, human activities have also played a role in the evolution of the territory.

As a first approximation, the broad study area (western Ferrara Province) consists of a gently ENE dipping topographic surface ranging between 20 m a.s.l. in the Cento area and ca. 4 m east of Ferrara. The mean slope is about 0.5‰, but the gradient can be as high as 5% where local topographic 'anomalies' are associated with active or abandoned levees or fluvial breaches. For the purposes of this study, most of the analysed benchmarks of the HPL network (Section 4) are located in correspondence to abandoned fluvial bodies. The following short description of the late Holocene hydrographic evolution is crucial for an understanding of the major geomorphic effects discussed in Section 5.

About 2500 years ago, the lowest sector of the Po River flowed across the present-day Ficarolo, Bondeno, Ferrara and Cona, forming the so-called *Po di Ferrara* (*a* in Fig. 2). In the same period, characterized by a generally warm climate, the Reno River flowed across the present-day San Pietro and Poggio Renatico (*b* in Fig. 2).

In the 6th–8th century A.D., the climate was particularly wet and the abundant precipitation caused hydrographic instability. During this period, the Po di Ferrara splits into the *Volano* and *Primaro* branches (*c* and *d* in Fig. 2, respectively), while the Reno River shifted westwards along a new course across Galliera (*e* in Fig. 2) and a few centuries later further west close to Pieve di Cento.

The restored warm conditions in the 9th–11th centuries favoured the expansion of farming within the plain, although in the 11th century the whole area suffered a critical hydrographic rearrangement due to several disastrous floods near Ficarolo which diverted the Po River (*Po Grande*) north of Ferrara (*f* in Fig. 2). This strong territorial reorganization was likely caused by the reactivation of the Casaglia blind thrust (Fig. 1) and consequent growth of the associated fault-propagation anticline.

In the following centuries, the water discharge of the southern branches of the Po River progressively decreased, inducing a gradual infill of the channels which was further worsened by the inflow of the Panaro River near Bondeno (*g* in Fig. 2). In the same period, the Reno River began to split into several channels (*h*, *i*, *l* and *m* in Fig. 2), distributing water and sediments in a broad area north of Cento (Bondesan et al., 1992).

Following the disastrous floods in 1451 and 1457 (Frizzi, 1848), the Reno River was artificially channeled between Cento and Pieve (*n* in Fig. 2) and it soon started to rapidly prograd (several kilometers in just a few years) toward Sant'Agostino and Vigarano Mainarda (*o* in Fig. 2), where it was left to freely flood and fill the area between Ferrara

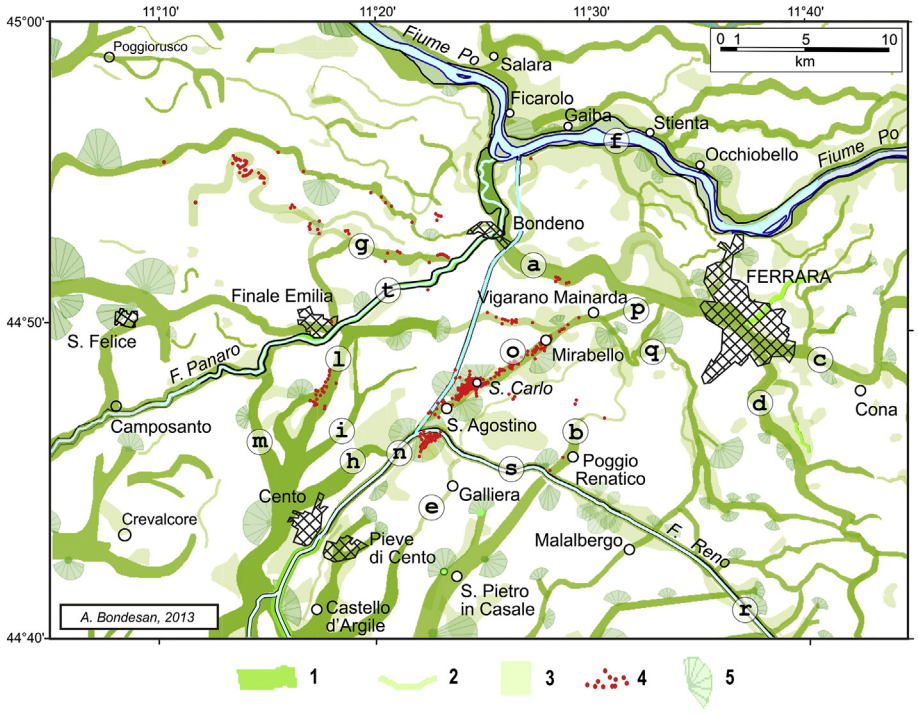

Fig. 2. Geomorphological sketch map of the broader epicentral area showing the complex hydrographic drainage developed in historical times as a consequence of tectonic activity, climatic changes and human interventions. See Fig. 1 for location. Letters indicate distinct branches of the Po, Reno and Panaro rivers referred to in the text. Legend: 1) palaeo- and active levees associated with a morphological relief; 2) palaeo-channels entrenched in the alluvial plain; 3) flooding areas characterized by sandy deposits; 4) surface evidence of liquefaction phenomena caused by the May 20, 2012 event; 5) major breaches and associated fan deposits.

and Poggio Renatico. In 1526, this branch of the Reno River was connected to the Po di Ferrara by means of a channel dug east of Vigarano (*p* in Fig. 2). This intervention drastically accelerated the infilling of the old Po channel causing as many as 40 floods in just 16 years and widespread swamping of the area around the town (Bottoni, 1873). As a consequence, this artificial connection was cut in the 17th century and the Reno River was diverted south-eastwards (*q* in Fig. 2) to induce land reclamation by sedimentary infilling (Roversi, 1989). At that time, the worsening climatic conditions (*i.e.* increased precipitation, water discharge and sediment transport) necessitated a progressive artificial elevation of the levees for many rivers crossing the area and a hydraulic management plan. For example, in order to drain the swampy area created SW of Ferrara, the *Cavo Benedettino* (*r* in Fig. 2) was excavated from 1724 to 1742, with partial exploitation of older river channels and in 1771–1775 the Reno River was diverted south-eastwards near Sant'Agostino (Franceschini, 1983) (*s* in Fig. 2). In the meantime, the Panaro River between Finale Emilia and Bondeno flowed along two courses, a natural branch and a partially artificial channel (*g* and *t* in Fig. 2, respectively), of which the former was abandoned at the end of the 19th century.

3. DInSAR technique

The DInSAR technique is based on the use of the phase component from two SAR images of the same area. Each SAR image consists of a real and an imaginary part, or equivalently, each pixel in a SAR image has an amplitude component and a phase component. The latter is related to the satellite-to-target distance, consisting of a large number of integer wavelengths and the measured fractional phase component. The result of DInSAR application is the so-called "interferogram", the pixel-to-pixel difference of the phase components of two SAR images covering the same area.

The interferometric phase Φ_{int} can be schematically split into five terms, the "flat earth" component Φ_f, the topographic phase Φ_{topo}, the displacement phase Φ_{displ}, the atmospheric term Φ_{atm}, and the error phase Φ_{err} (Massonnet and Feigl, 1998). The first term deals with the SAR acquisition geometry and can be easily removed thanks to the very precise knowledge of the orbital position and trajectory. The topographic phase is related to the normal baseline which is the projection of the distance between the two positions of the satellite, looking at the same region at different times, onto the direction orthogonal to the line of sight (hereafter LOS; *i.e.*, the line from the sensor to the target on the surface). Finally, displacements occurring on the ground surface and causing changes in the sensor-to-ground distance result in the phase variation (Φ_{displ}). In order to highlight this phase change due to displacement, the "flat earth" and topographic terms have to be removed (the latter generally using an independently determined digital elevation model). Actually, the name DInSAR refers to the technique applied to generate such topographically corrected interferograms. This technique measures the projection of the displacement vectors (North, East and Up components of three-dimensional surface displacements) along the satellite LOS. The interferogram is calculated as the modulo 2π phase difference, because of the nature of complex numbers. To obtain an LOS displacement map, the result of DInSAR should be moved from the wrapped discontinuous interference signal to the unwrapped continuous phase difference. Phase unwrapping is often a critical step in the estimation of ground displacement, and if an interferogram is strongly affected by noise, the lack of signal continuity (decorrelation) may introduce errors in the displacement values (unwrapping errors). Such errors can sometimes be mitigated using independent observations, such as GPS, leveling data, or other interferograms from different orbits or satellites.

To study the surface deformation caused by the May 20 and May 29 events, we applied the DInSAR technique to two pairs of SAR images. The first image pair was acquired by the Canadian satellite RADARSAT-1 (RS1), a C-band SAR, on descending orbit. The pre-event RS1 image is dated May 12, 2012, few days before the first mainshock, while the second image was acquired on June 5. Hence the time span covered embraces the two main shocks and several aftershocks including five events with M_w greater than 5. The RS1 pair has a perpendicular

(spatial) baseline of 309 m and a temporal baseline of 24 days. The topographic phase contribution was removed using the Shuttle Radar Topographic Mission (SRTM; Farr et al., 2007) DEM. In addition, the Goldstein filter (Goldstein and Werner, 1998) was applied in attempt to increase the signal-to-noise ratio to allow a more accurate unwrapping of the phase.

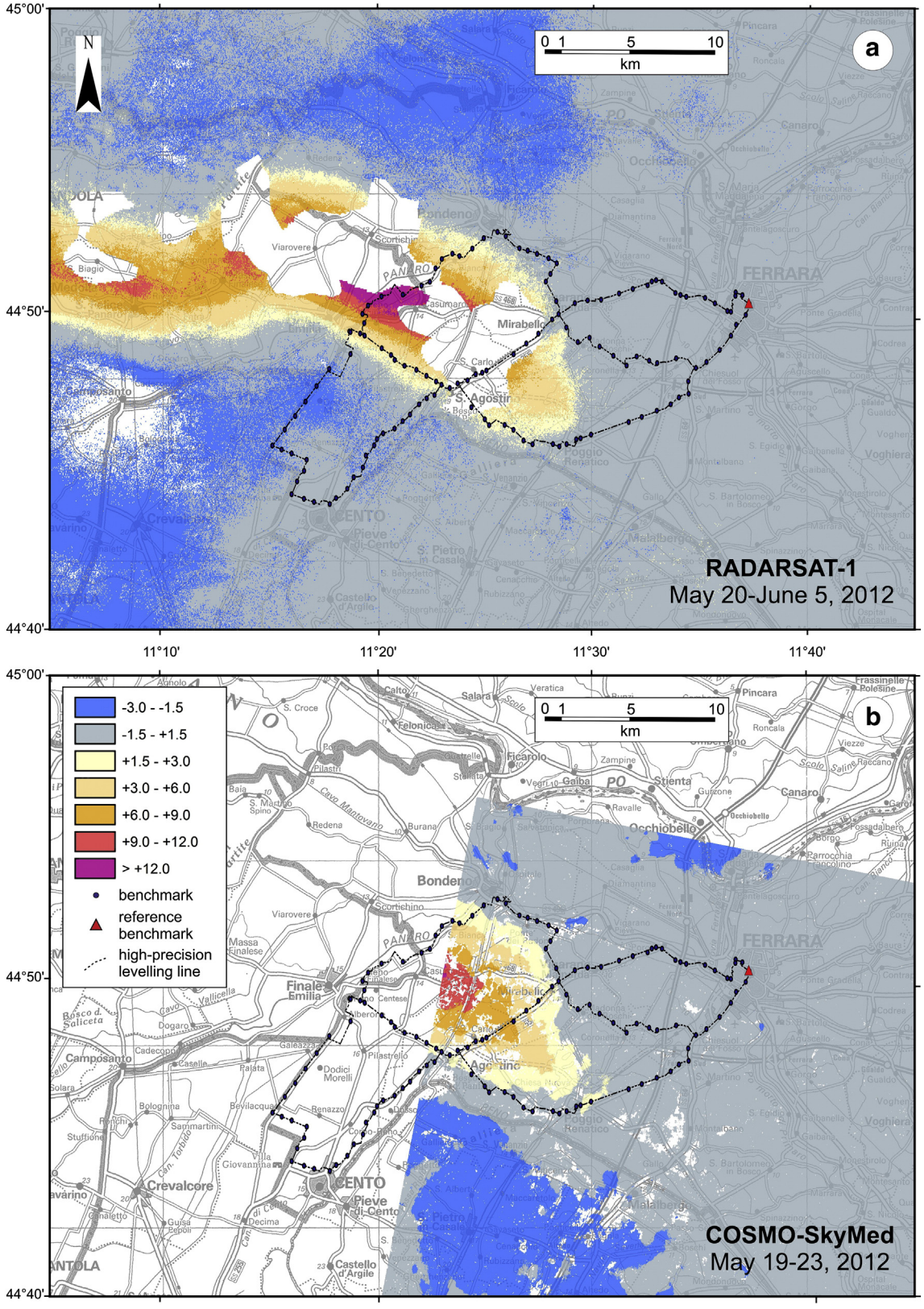

Fig. 3. DInSAR results applied to a) Canadian RADARSAT-1 satellite data (C-band SAR on descending orbit) and b) European COSMO-SkyMed-1 satellite data (X-band SAR on descending orbit). See Fig. 1 for location. In (a) the paired images are dated May 12 and June 5, 2012 and thus document the deformation associated with both mainshocks (May 20 and 29). Note the distinct (though partially overlapping) effects of the two principal morphogenic earthquakes. In (b) the paired images are dated May 19 and May 23, 2012 and thus document the deformation associated only with the first mainshock (May 20). The HPL lines discussed in Section 4 are also shown.

The resulting deformation map (Fig. 3a) shows a region characterized by movement toward the satellite (an uplift), reaching a maximum displacement of about 17 cm in the LOS direction, in this case corresponding to 34° off the nadir viewing angle. Two connected and partially overlapping sectors within the study area show a marked displacement which is a clear effect of the (mainly) coseisco-seismic activity of the two causative faults associated with the May 20 (eastern sector, $M_w = 6.1$) and May 29 (western sector, $M_w = 5.9$) mainshocks. A relatively small subsidence, up to a peak value of about 3 cm, was also detected in the southern area close to the western sector.

A second SAR image pair, also on descending orbit, was available from the Italian X-band SAR mission COSMO-SkyMed (CSK). The two images are dated May 19 and May 23, 2012, hence with four days separation and a perpendicular baseline of 366 m. This image pair encompasses only the first of the two main shocks.

Also for the CSK data the interferometric phase component related to the topography was removed using the SRTM DEM, and the Goldstein filter was applied to recover the loss of interferometric coherence due to local effects such as the liquefactions. With this approach we were able to keep the record of tectonics and large scale topographic deformation.

Fig. 3b shows the displacement map obtained from the DinSAR processing of the CSK images. As observed in the RS1 interferogram, we detected a region with a maximum positive movement (toward the satellite) in the LOS direction of about 13 cm. The lower displacement with respect to the RS1 interferogram is partly due to coverage of the CSK data frame only in the eastern sector of the epicentral area of the May 20 event, thus missing the sector with the largest values. However, because of the different time spans considered in the second interferogram, the larger surface displacement inferred from the RS1 is partly due to a prolonged post-seismic deformation effect.

4. Levelling

Ferrara Province is characterized by a low mean ground elevation a.s.l. and, for large sectors, even below the sea level. As briefly mentioned in Section 2, several drainage works have been carried out over the past few centuries. At present, accurate knowledge of the topography of the area is crucial for better drainage management. For this purpose, several permanent levelling networks were established through the territory many years ago. The creation of these networks and their repeated measurement are the principal 'mission' of the "Consorzio di Bonifica Pianura di Ferrara" (hereafter "Consortium") whose activities are part of the Geographic Information System sector. A "first order" geometric leveling network covering the whole area was realized between 2005 and 2012. The network provides a high accuracy local vertical datum and consists of about 1200 km of levelling lines across Ferrara Province with an average levelling section length of about 1 km.

For the survey of the network, we applied the international standards for high-precision geometric levelling. In particular, we established a maximum allowed discrepancy of $\pm 2.5\sqrt{\ell}$ mm in double-run levelling where ℓ is the length of the levelling segment in km, and a maximum value for ring closure of $\pm 2.5\sqrt{L}$ mm, where L is the length of the ring in km.

Since the first DInSAR results (Bignami et al., 2012; Salvi et al., 2012) concerning the two major Emilia 2012 earthquakes, a significant and broad uplift of the ground was recognised (Fig. 3). The eastern sector of the area affected by uplift is crossed by the levelling network of the Consortium and for the purpose of this research we carried out a dedicated survey along selected lines for a total length of about 120 km (Fig. 4) in the months following the seismic crisis. The levelling network was measured with two Topcon DL101C digital levels with INVAR staffs (standard deviations 0.4 mm km^{-1} in double-run levelling). The adjustment of the measurements was performed by the classic least squares method. The resulting standard error of the adjusted height differences is ± 1.14 mm km^{-1}, while the standard deviation of the adjusted heights is less than 5 mm.

The reference benchmark (point "A" in Fig. 4) belongs to the Italian First Order Levelling Network surveyed in 2005 by the IGM (Istituto Geografico Militare). Accordingly, all the heights are referred to the national vertical datum. Since the Ferrara national benchmark (precisely re-determined in 2005) is at an epicentral distance of ca. 25 km and no permanent co-seismic deformation has ever been recorded for similar magnitude events at such distances, we assumed its height as the vertical datum. Moreover, the DInSAR technique confirmed the lack of detectable vertical deformation at the Ferrara site (see Section 3 and Fig. 3). The assumption of a 'stable' benchmark is further supported by the fact that the height of all secondary benchmarks of the levelling line closest to the reference benchmark (Ferrara) remained almost unchanged when the pre- and post-earthquake measurements were compared (Fig. 5).

The heights of the benchmarks were compared by obtaining the vertical movements of the ground during the time interval between the two HPL campaigns carried out before (March–September 2009) and after (September 2012–June 2013) the seismic sequence. The analysis of the vertical movements revealed both uplifted and subsided benchmarks. The levelling lines re-measured after the seismic sequence could be grouped into three main sets on the basis of their different orientation and location as well as different behaviour in terms of vertical recorded movements. For example, the three levelling lines closest to Ferrara (*i.e.* farthest from the epicentre), with a mean E–W orientation (Fig. 5) show remarkable temporal stability. A light but systematic uplift of 1–2 cm is suggested only in the western part of the D–E line, which is relatively close to the epicentral area (Fig. 5c). There are a few appreciable exceptions to this otherwise regular distribution of vertical movements near Mirabello (Fig. 5a,b) where a marked subsidence (up to ca. 10 cm) was measured. The behaviour of these benchmarks will be discussed in the following section.

A second set of levelling lines (Fig. 6) corresponds to three paths closest to the epicentral area with a mean ESE–WNW orientation, thus roughly parallel to the seismogenic fault's strike associated with the morphogenic event of May 20th. Also in this case, there is a uniform behaviour of the single levelling lines, albeit variable from north to south. Indeed, the northern line (C–B in Fig. 6) shows no vertical movements, the southern one (G–H in Fig. 6) a slight subsidence of ca. 2 cm all along its length, while the intermediate one (F–D in Fig. 6) clearly indicates a general uplift between 3 and 6 cm. This general picture, characterized by vertical stability in an ESE–WNW direction and lateral variations in a NNE–SSW direction is also clearly shown by the levelling line G–F–C (Fig. 7a) where the maximum uplift values were observed. The vertical movement of the benchmarks gradually varies along this line: there is a slight subsidence in the southern sector (1–2 cm), which is smoothly inverted in the central sector south of Finale Emilia to become a positive vertical movement (*i.e.* uplift) that progressively increases up to the maximum value reached at about 15 km (north of Finale Emilia). Farther northwards, the displacement of the benchmarks decreases to a few centimeters of uplift at Bondeno (Fig. 7a). If we project the values along a NNE–SSW straight line, it is possible to estimate a wavelength of about 10 km for the fold deforming the topography.

5. Major geomorphic effects: liquefaction and local subsidence

The May 2012 Emilia events were characterized by spectacular and locally very intense liquefaction phenomena (*e.g.* Caputo and Papathanasiou, 2012; Papathanassiou et al., 2012) that possibly mobilized shallow, but in some places large, sedimentary volumes. As a consequence, ground deformations were induced at different scales involving areas from a few meters to several hundred meters in size; they caused horizontal movements up to several centimeters (*i.e.* lateral spreading), and both positive and negative vertical movements, the latter generally much more frequent and locally exceeding some tens of centimeters. These effects on the earth's surface occurred with a

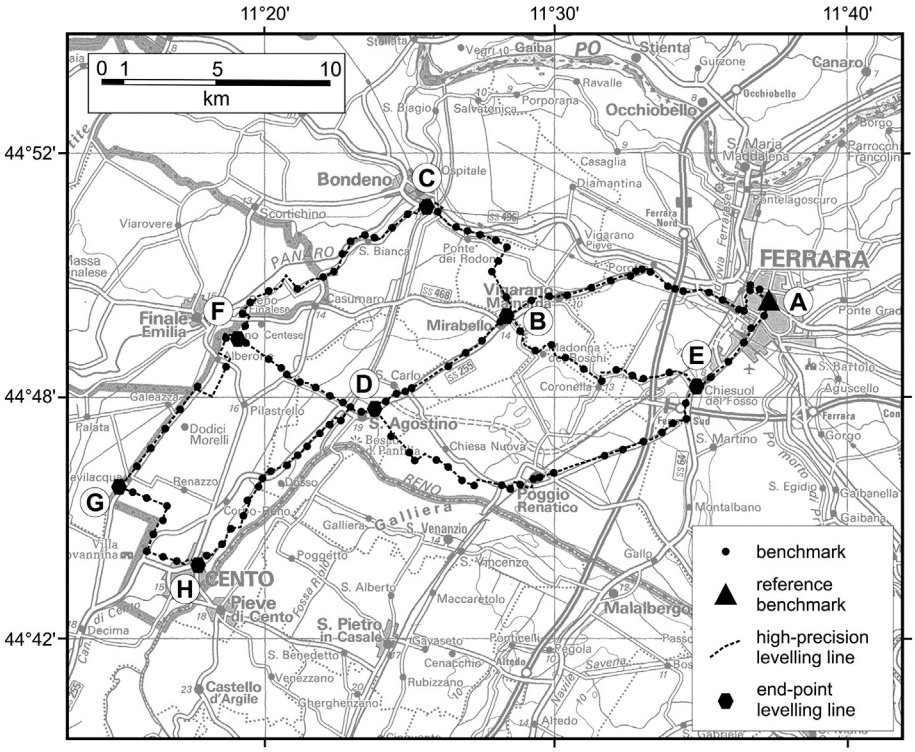

Fig. 4. The first order levelling network belonging to the "Consorzio Pianura di Ferrara", Ferrara Province, which was re-measured following the 2012 seismic sequence. Small dots represent the benchmarks of the Consortium, the hexagons represent the labelled benchmarks discriminating the levelling lines, while the triangle is the reference benchmark belonging to the Italian First Order Levelling Network, re-surveyed in 2005 by the IGM (Istituto Geografico Militare).

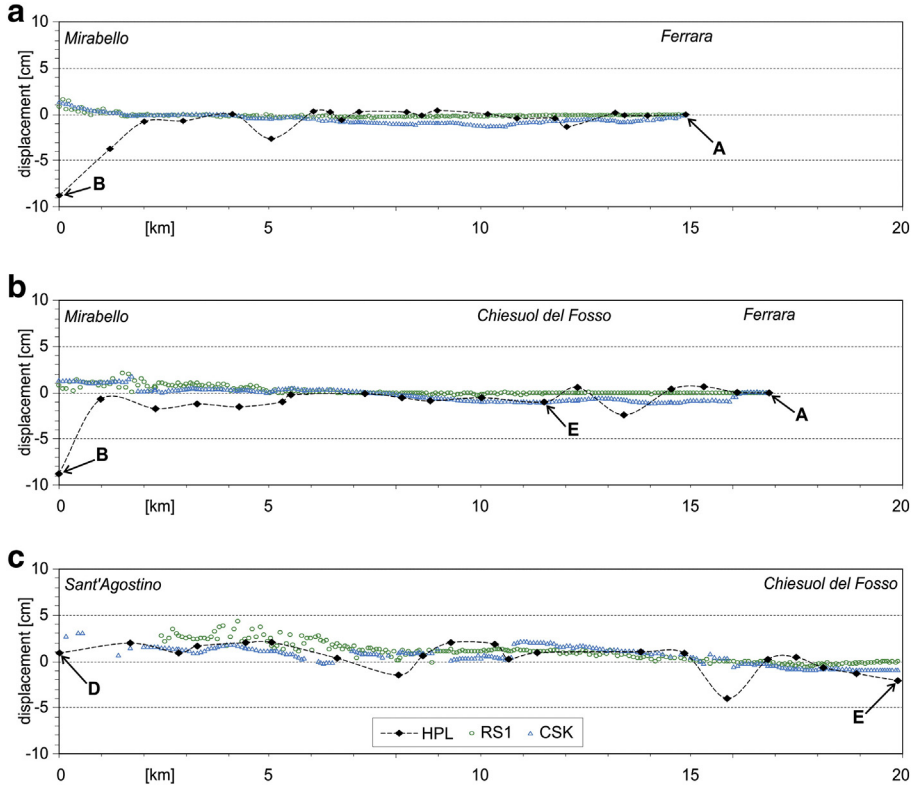

Fig. 5. Vertical movements measured along the three levelling lines closest to Ferrara (*i.e.* farthest from the epicentre), with a mean E–W orientation and showing remarkable stability. The error bar at each benchmark calculated on the basis of the standard deviations of the differences in elevation (pre- to post-earthquake) is smaller than the symbol size. Capital letters refer to the benchmarks labelled in Fig. 4. HPL: high-precision levelling; RS1: RADARSAT-1; CSK: COSMO-SkyMed.

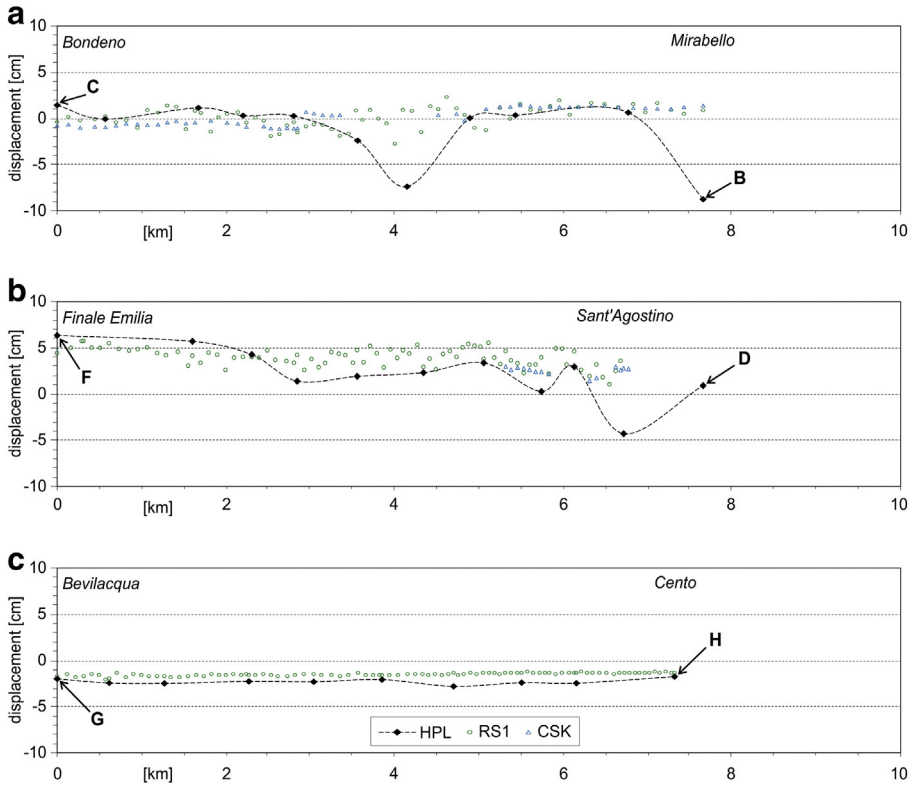

Fig. 6. Vertical movements measured along the three levelling lines closest to the epicentral area with a mean ESE–WNW orientation showing a uniform behaviour of the single levelling lines, albeit variable from north to south. The error bar at each benchmark calculated on the basis of the standard deviations of the differences in elevation (pre- to post-earthquake) is smaller than the symbol size. Capital letters refer to the benchmarks labelled in Fig. 4. HPL: high-precision levelling; RS1: RADARSAT-1; CSK: COSMO-SkyMed.

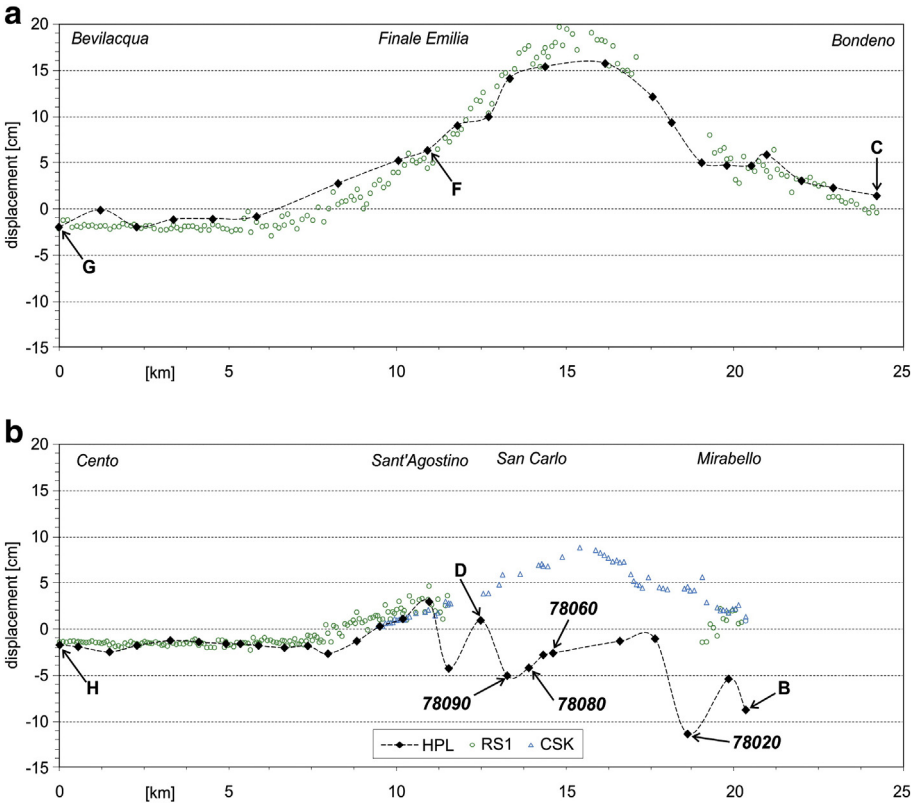

Fig. 7. Vertical movements measured along the two levelling lines running perpendicular to the May 20 fault strike. Profile G–F–C (a) well reproduces the satellite results, while profile H–D–B shows some marked differences with strongly subsided benchmarks. The error bar at each benchmark calculated on the basis of the standard deviations of the differences in elevation (pre- to post-earthquake) is smaller than the symbol size. Capital letters refer to the benchmarks labelled in Fig. 4. HPL: high-precision levelling; RS1: RADARSAT-1; CSK: COSMO-SkyMed.

jeopardized pattern, thus influencing both terrestrial and satellite-based techniques, albeit in different ways.

For the HPL, this effect is particularly evident along the levelling line H–D–B (Fig. 7b). Indeed, it runs parallel to the previously described line G–F–C (Fig. 7a), showing both similarities and marked differences. For example, there are similarities in the southern and central sectors, where all the benchmarks from south to north show a quite constant subsidence value (ca. 2 cm) that progressively changes into positive vertical movements (up to 3 cm of uplift near Sant'Agostino). The G–F–C line continues to show regular uplifting northwards, as shown by the SAR displacements, In the H–D–B line instead the benchmarks deviate from a regular trend from San'Agostino (point D) onwards, showing highly variable vertical displacements with mainly negative values. Indeed, between San Carlo and Mirabello, the subsidence is locally as great as 11.4 cm (Fig. 7b). As already discussed that interferometric processing, was performed to preserve the large-scale tectonic signal; therefore, these local subsidences were smoothed out. We analyzed various possible causes in order to explain i) these discrepancies with respect to the relatively nearby and parallel profile (G–F–C), ii) the locally high subsidence values (up to −11.4 cm) and iii) the very short wavelength of the vertical variations.

Firstly, it must be noted that the benchmark displacement could include the effect of long-term vertical movements during the period between the two campaigns (2005–2012). However, the available data (http://www.arpa.emr.it/dettaglio_notizia.asp?id=4801&idlivello=1414, in Italian, last visited April 28, 2014) suggest that the 'regional' subsidence affecting the broader region of the lower Po Plain during this time span (and also recorded at the reference benchmark of Ferrara) was less than 1 to 2 cm. Above all no significant gradients have been documented so far within the study area. Hence we can exclude a long-term effect as the cause of the local, albeit strongly, subsided benchmarks and the difference between the high-precision levelling and satellite interferometry results.

Secondly, we analysed in detail the geological setting of the sites where the 'anomalous' benchmarks were installed. Indeed, immediate post-event surveys following the May 20 earthquake documented diffuse liquefaction phenomena in this sector of the plain (Fig. 2; *e.g.* Papathanassiou et al., 2012; Caputo and Papathanasiou, 2012).

Information on the shallow subsoil close to each benchmark was derived from drill cores, penetration tests and water wells. Although we performed a similar analysis for all controversial benchmarks, we will discuss here only a few remarkable examples to understand the above-mentioned 'anomalous' behaviour observed along the levelling line. For example, benchmark 78020 (yellow star in Fig. 8a), located at the entrance of the Mirabello cemetery, showed a subsidence of 11.4 cm (Fig. 7b). The cemetery area is located along a palaeo-branch of the Reno River (location *o* in Fig. 2) and particularly at the base of the south-eastern slope of the left levee (Fig. 8a). The shallow stratigraphy observed in some drill cores around the benchmark (black stars in Fig. 8a) consists of alternating fine silty sand and saturated sandy silt in the first 5 to 6 m overlying a thick body of medium-grained sand. These are typical conditions prone to liquefaction in the case of seismic shaking. Indeed, during the May 20 event, the broader cemetery area was affected by several ground effects associated with, and induced by, widespread liquefaction phenomena. In particular, several ground deformations occurred co-seismically (red squares in Fig. 8a,d) a few meters from benchmark 78020, clearly documenting the local loss of shear resistance within the subsoil which certainly reacted differentially as a function of the vertical loads. The benchmark is cemented next to the heavy entrance pillar of the cemetery boundary wall, which very likely suffered some settling, thus also displacing the benchmark. Moreover, large amounts of liquefied sand were ejected within the broader area (blue dots in Fig. 8a) and this necessarily caused further subsidence due to the consequent compaction and volumetric reduction of the underlying sandy layer(s). In addition to the 'local' effects, the whole southeastern slope of the levee suffered large-scale lateral spreading (Fig. 8a,b); the sliding surface likely exploited gently dipping sandy forests well documented within the same levee body a few kilometers to the south within a palaeo–seismological trench (Caputo et al., 2012). Accordingly, the lateral spreading also induced a vertical component of motion (Fig. 8c), which certainly contributed to the subsidence of benchmark 78020 (−11.4 cm). Similar phenomena were documented by Pizzi and Scisciani (2012).

A second example is represented by benchmark 78060, located on the base of a tall lamp post in the centre of the roundabout at the northern entrance to San Carlo (Fig. 9a,b). Drill-cores and CPTs (cone penetration tests) carried out a few tens of meters from the benchmark clearly show the presence of saturated fine silty sands at 4 to 6 m depth. Based on the CPTs and the approach proposed by Idriss and Boulanger (2008), it was also possible to calculate a liquefaction potential index (*LPI*; Iwasaki et al., 1978) of 10.5, which corresponds to a high liquefaction risk (Sonmez, 2003). Moreover, widespread sand ejections were observed in the surroundings during the immediate post-event survey (Fig. 9c; Caputo and Papathanasiou, 2012). Considering the combined weight of the metal pole and its foundation (roughly 1 m^3 of concrete), some amount of permanent settling induced by the coseisco-seismic liquefaction would be expected and could reasonably explain the 2.8 cm of subsidence measured at this benchmark (Fig. 7b).

Benchmark 78080 located on the bike lane along the provincial road at San Carlo (Fig. 9a), showed a subsidence of 4.4 cm (Fig. 7b). CPTs carried out close to the benchmark clearly documented a saturated sandy silt layer at 4.5 to 5.5 m depth and a moderate *LPI* value. Interestingly, a few tens of meters away from the benchmark, a water well was apparently uplifted by ca. 8 cm, thus coming out of its case (Fig. 9e); the metal rod is rooted at 30 m-depth, suggesting that the nearby ground has permanently subsided as a consequence of the dewatering, sand ejection and hence compaction as observed in the surroundings.

Benchmark 78090 also showed a subsidence of 5.3 cm (Fig. 7b). As at Mirabello (Fig. 8), this benchmark is fixed at the entrance of a cemetery located along the same palaeo-branch of the Reno River (location *o* in Fig. 2), although in this case at the base of the external slope of the right levee (Fig. 9a). Here lateral spreading and diffuse sand ejection also occurred in concomitance with the May 20 event (respectively white arrows and blue dots in Fig. 9a), while geotechnical results and palaeoseismological excavations (Caputo et al., 2012) confirmed the presence of a thick layer of saturated fine-medium sands between 4 to 8–8.5 m depth. As a consequence both horizontal and vertical movements were induced (Figs. 7b and 9d), explaining the measured subsidence and allowing us to classify this as a local effect.

6. Discussion

To best exploit all the available information on ground motion, we compare the results of i) HPL (Section 4), ii) DInSAR analyses (Section 3), iii) distribution of the 2012 liquefaction phenomena (Papathanassiou et al., 2012); iv) a geomorphological map of the area (M.U.R.S.T., 1997) and v) the structural model of the region providing information about the depth of the bedrock (Bigi et al., 1990).

The interferograms clearly define a large sector of the alluvial plain characterized by an elliptical geometry affected by a marked uplift. This occurs in correspondence with the crest of a fault-propagation fold associated with the causative source of the May 20 Emilia event. The satellite analyses also show two broad areas affected by a slight subsidence north and south of the anticline (Fig. 3) in perfect agreement with elastic deformation models (*e.g.* Okada, 1985; Burrato et al., 2003). Calculation of the vertical movement from the LOS azimuthal angle, gives a maximum observed uplift of ca. 17 cm near Casumaro, while the amount of subsidence is always less than 3 cm. Although the pair of RS1 images embraces a time span including both major earthquakes, the area uplifted by the May 20 event is clearly recognisable and measures about 27 km in length and almost 10 km

Fig. 8. Geomorphological features observed in Mirabello the area (see Fig. 2 for location): a) Google Earth frame of the cemetery area showing the distribution of secondary co-seismic effects, such as sand ejection points (blue dots), ground deformation sites (red squares), drill cores (black stars), ground ruptures (yellow arrows) and sliding direction due to lateral spreading (white arrows). The yellow star indicates the location of benchmark *78020* characterized by 11.4 cm of subsidence. b) Ground ruptures observed on top of the abandoned levee (see (a) for location). c) Effects of the lateral spreading on the lateral wall of the cemetery (see (a) for location). d) Example of ground deformation associated with shallow liquefaction (see (a) for location). (For interpretation of the references to color in this figure legend, the reader is referred to the web version of this article.)

in width (ESE–WNW and NNE–SSW, respectively). This surface deformation has also been described and modelled by Pezzo et al. (2013).

Since the CSK 'captured' only the first mainshock and the RS1 both major events, we also attempted to analyse the possible effects accumulated during the post-seismic deformation of the first major shock. Taking into account the different qualities of the images and the characteristics of the two satellites, we conclude that the comparison does not show the occurrence of post-seismic effects, or at least the induced LOS variations are below the resolution of the two methods.

One of the major aims of this research was a comparison of the results of HPL and the DInSAR technique. In this regard, there is perfect agreement among Figs. 5, 6 and particularly 7a, where the pattern of vertical movements obtained from the two approaches mimic each other. Moreover locally the two techniques are almost complementary. For example, along the profile G–F–C (Fig. 7a), satellite information is missing between Finale Emilia and Bondeno because the results show no coherence. Conversely, along the profile H–D–B (Fig. 7b), several HPL benchmarks north of Sant'Agostino were affected by local co-seismic effects, showing anomalous subsidence values which do not reflect the large-scale tectonically induced surface deformation. In this case the satellite data fill the information gap.

A second major goal of this work was a comparison of our results with the tectonic setting of the region corresponding to the central-western part of the complex Ferrara Arc representing the frontal and buried sector of the Northern Apennines orogenic wedge (Fig. 1). The uplifted areas documented in this paper clearly reflect the reactivation of blind thrusts representing distinct seismogenic segments and help to better constrain their geometry and kinematics. On the other hand, the cumulative Quaternary effects are also emphasized by the important lateral variations in thickness of the coeval deposits (*e.g.* Martelli and Molinari, 2008). The most recent activity is also suggested by several hydrographic anomalies observed in the epicentral area (*e.g.* Burrato et al., 2012), such as the divergence of two palaeochannels near Finale Emilia (*g* and *l* in Fig. 2), the progressive infilling and abandonment of the Sant'Agostino to Mirabello branch of the Reno River (*o* in Fig. 2) and its older paths (*b* and *e* in Fig. 2) as well as the recent diversion (*s* in Fig. 2) (see Section 2).

7. Concluding remarks

In the present study we analysed in detail the geodetic information available for a wide sector of the M_w 6.1 Emilia 2012 epicentral area

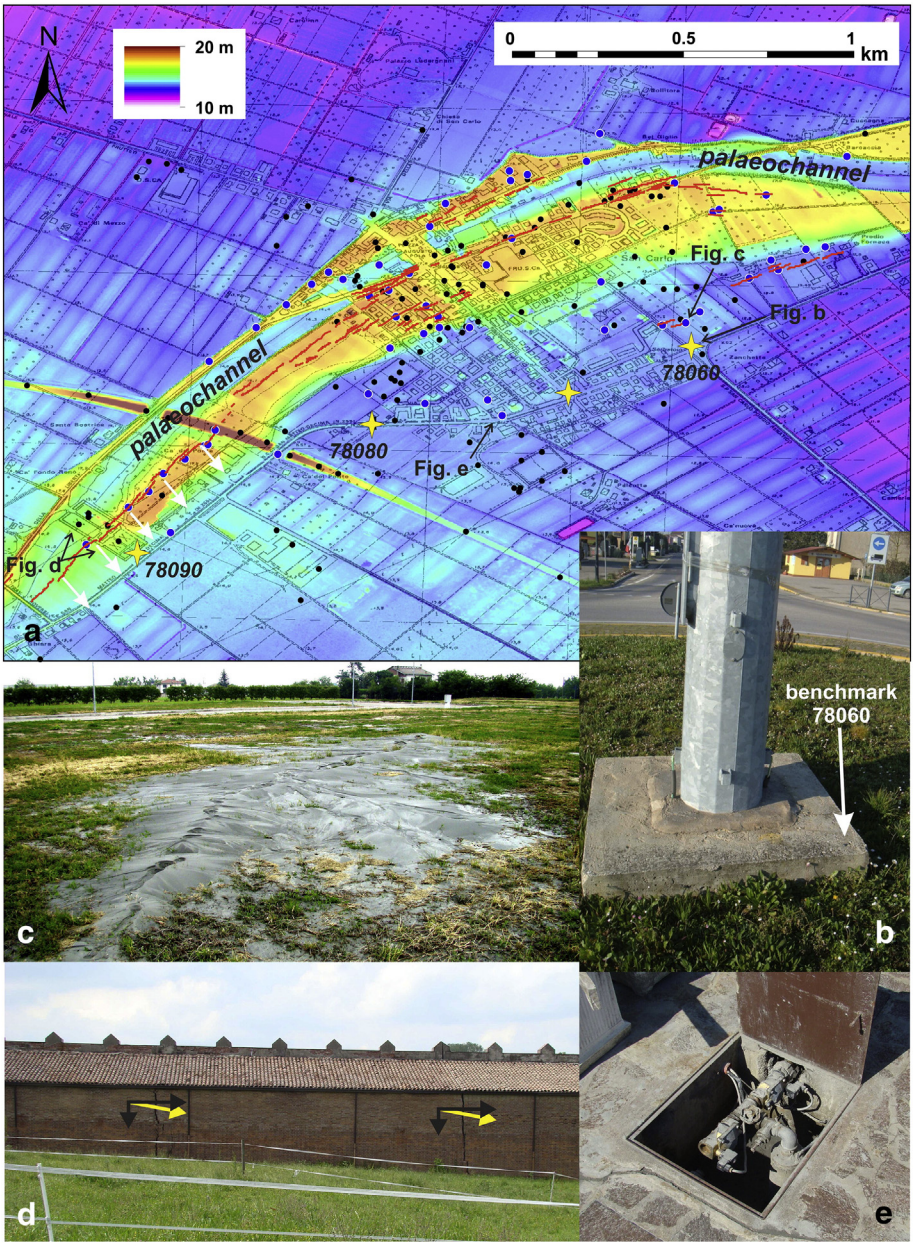

Fig. 9. Geomorphological features observed in the San Carlo area (see Fig. 2 for location): a) Digital elevation model clearly showing the two levees of the palaeo-Reno River. Red lines represent the major ground ruptures observed after the May 20 event (Caputo and Papathanasiou, 2012) generally associated with lateral spreading phenomena (white arrows). Blue dots are sand ejection points while black ones are penetration tests providing information about the shallow subsoil. Yellow stars are benchmarks of the HPL line. b) The foundation of the lamp post installed in the center of the roundabout at the northern entrance to San Carlo where diffuse liquefaction has occurred (c) (see (a) for locations). d) The southern wall of the cemetery built on the slope of the palaeolevee and affected by lateral spreading contributing to the subsidence of benchmark 78090. e) Example of a water well located close to benchmark 78080, which was apparently uplifted ca. 8 cm relative to the ground surface, thus coming out off its case. See text for discussion. (For interpretation of the references to color in this figure legend, the reader is referred to the web version of this article.)

(Figs. 1 and 3). In particular, we separately analysed i) HPL lines surveyed before (March–September 2009) and after (September 2012–June 2013) the seismic sequence, and ii) two pairs of SAR images acquired by, the RS1 and CSK satellites; for the former the DInSAR technique was applied to frames dated May 12 and June 5, while for the latter the frames are dated May 19 and 23. Although the time span of the RS1 interferogram includes both mainshocks (May 20 and 29) of the seismic sequence, the epicentral uplifted area of the second event lies outside the region we focused on, corresponding to the eastern sector of the first earthquake, and thus did not influence our analysis.

A second important part of our research is the comparison of the results of the terrestrial and satellite approaches (Figs. 5, 6 and 7). This showed the excellent qualitative and quantitative agreement, between the two methods of investigating vertical movements. Moreover, we found that locally the two techniques are almost complementary. Indeed, in a sector where the satellite information was missing due to the lack of coherence (Figs. 3 and 7a), HPL allowed us to determine the ground deformation. On the other hand, the anomalous vertical movements (*i.e.* subsidence) measured in some HPL benchmarks and caused by local liquefaction phenomena did not reflect the large-scale tectonic signal and the results of satellite technique compensated for this missing or biased information.

In conclusion, the major outcomes of the present study are twofold. Firstly, the results obtained independently from different geodetic approaches provide valuable information about the co-seismic soil deformation induced by the Emilia 2012 earthquakes which will help

to better constrain some of the principal seismotectonic parameters of the reactivated faults. In this regard, several examples in the literature show the importance, for a better definition of seismogenic sources, of geodetic information based on terrestrial levelling (*e.g.* Burford, 1972; Stein et al., 1988; Lin and Stein, 1989; Gahalaut et al., 1994; Clarke et al., 1997) or satellite interferograms (*e.g.* Meyer et al., 1998; Kontoes et al., 2000; Cakir et al., 2006; Atzori et al., 2008; Ilieva, 2011; Li et al., 2011; Wang et al., 2012; Pezzo et al., 2013).

Secondly, we document how widespread liquefaction phenomena, induced by seismic shaking affecting recent clastic and saturated deposits, can strongly influence the local elevations even completely reversing the large-scale tectonic signal (*i.e.* from uplift to absolute subsidence). Although this conclusion might be intuitive, to our knowledge this is the first time that tectonic deformation *versus* site effects have been rigorously compared and analysed. The importance of this resides in the fact that the geological and seismotectonic conditions characterizing the Emilia 2012 epicentral area occur in many other regions worldwide. As a final comment on this point, we stress the lesson learned in relation to the topology of HPL networks and particularly concerning the location of the benchmarks. It is obvious that such monitoring systems must be located for practical reasons along major road axes, which in alluvial plains commonly run on top of artificial embankments or natural levees. In the case of moderate-to-strong seismic shaking, both earthworks and sedimentary bodies easily undergo diffuse settling and liquefaction (Fig. 2). If no alternative siting is available for HPL lines, network planners should be aware of the intrinsic risk of 'loosening' some of the benchmarks. Strategic precautions could be the positioning of a (much) denser network or the use of more stable installation techniques, such as connecting the benchmark to a rod driven below the liquefaction depth. In the former case, the chance of preserving correct measurements along the line increases, while using a deeper foundation of selected benchmarks could avoid the effects of liquefaction which are potentially devastating for HPL networks.

Acknowledgments

We thank the two anonymous reviewers and the Editor Takashi Oguchi for their comments that improved the manuscript. The contribution of Marco Ardizzoni, Bruno Desiderati and Nicola Astolfi to the high precision levelling campaigns is warmly acknowledged.

References

Atzori, S., Manunta, M., Fornaro, G., Ganas, A., Salvi, S., 2008. Postseismic displacement of the 1999 Athens earthquake retrieved by the Differential Interferometry by Synthetic Aperture Radar time series. J. Geophys. Res. 113, B09309. http://dx.doi.org/10.1029/2007JB005504.

Basili, R., Valensise, G., Vannoli, P., Burrato, P., Fracassi, U., Mariano, S., Tiberti, M.M., Boschi, E., 2008. The Database of Individual Seismogenic Sources (DISS), version 3: summarizing 20 years of research on Italy's earthquake geology. Tectonophysics 453 (1–4), 20–43. http://dx.doi.org/10.1016/j.tecto.2007.04.014.

Bigi G., Cosentino D., Parotto M., Sartori R. and Scandone P. (1990): Structural Model of Italy: Geodynamic project, C.N.R. Firenze, S.EL.CA., scale 1:500.000, sheets 1 and 2.

Bignami, C., Burrato, P., Cannelli, V., Chini, M., Falcucci, E., Ferretti, A., Gori, S., Kyriakopoulos, C., Melini, D., Moro, M., Novali, F., Saroli, M., Stramondo, S., Valensise, G., Vannoli, P., 2012. Coseismic deformation pattern of the Emilia 2012 seismic sequence imaged by Radarsat-1 interferometry. Ann. Geophys. 55 (4), 788–795. http://dx.doi.org/10.4401/ag-6157.

Bondesan, M., Ferri, R., Graziani, S., 1992. Aspetti geomorfologici e problemi paleogeografici della zona fra Bondeno, Finale Emilia e Mirabello nel quadro degli antichi domini idrografici del Secchia, del Panaro e del Reno. In: Gelichi, S. (Ed.), Un mito e un territorio: Ansalaregina e l'Alto Ferrarese nel Medioevo. Ed. All'insegna del Giglio, Firenze, pp. 13–44.

Bottoni, A., 1873. Appunti storici sulle rotte del basso Po dai tempi romani a tutto il 1839. Tip. Sociale, Ferrara.

Burford, R.O., 1972. Continued slip on the Coyote Creek fault after the Borrego Mountain earthquake. In: Sharp, R.V. (Ed.), The Borrego Mountain earthquake of April 9, 1968. Geol. Survey Professional Paper 787, pp. 105–111.

Burrato, P., Ciucci, F., Valensise, G., 2003. An inventory of river anomalies in the Po Plain, northern Italy: evidence for active blind thrust faulting. Ann. Geophys. 46 (5), 865–882.

Burrato, P., Vannoli, P., Fracassi, U., Basili, R., Valensise, G., 2012. Is blind faulting truly invisible? Tectonic-controlled drainage evolution in the epicentral area of the May 2012, Emilia-Romagna earthquake sequence (northern Italy). Ann. Geophys. 55 (4), 525–531. http://dx.doi.org/10.4401/ag-6182.

Cakir, Z., Meghraoui, M., Akoglu, A.M., Jabour, N., Belabbes, S., Ait-Brahim, L., 2006. Surface deformation associated with the Mw 6.4, 24 February 2004 Al Hoceima, Morocco, earthquake deduced from InSAR: implications for the active tectonics along North Africa. Bull. Seism. Soc. Am. 96 (1), 59–68. http://dx.doi.org/10.1785/0120050108.

Caputo, R., 2005. Ground effects of large morphogenic earthquakes. J. Geodyn. 40 (2–3), 113–118.

Caputo, R., Papathanasiou, G., 2012. Ground failure and liquefaction phenomena triggered by the 20 May, 2012 Emilia-Romagna (Northern Italy) earthquake: case study of Sant'Agostino — San Carlo — Mirabello zone. Nat. Hazards Earth Syst. Sci. 12 (11), 3177–3180. http://dx.doi.org/10.5194/nhess-12-3177-2012.

Caputo, R., Iordanidou, K., Minarelli, L., Papathanassiou, G., Poli, M.E., Rapti-Caputo, D., Sboras, S., Stefani, M., Zanferrari, A., 2012. Geological evidence of pre-2012 seismic events, Emilia-Romagna, Italy. Ann. Geophys. 55 (4), 743–749. http://dx.doi.org/10.4401/ag-6148.

Clarke, P.J., Paradisis, D., Briole, P., England, P.C., Parson, B.E., Billiris, H., Veis, G., Ruegg, J.-C., 1997. Geodetic investigation of the 13 May 1995 Kozani–Grevena (Greece) earthquake. Geophys. Res. Lett. 24 (6), 707–710.

DISS Working Group, 2010. Database of Individual Seismogenic Sources (DISS), Version 3.1.1: A Compilation of Potential Sources for Earthquakes Larger Than M 5.5 in Italy and Surrounding Areas. http://dx.doi.org/10.6092/INGV.IT-DISS3.1.1 (http://diss.rm.ingv.it/diss/, © INGV 2010 — Istituto Nazionale di Geofisica e Vulcanologia — All rights reserved).

Farr, T.G., Rosen, P.A., Caro, E., Crippen, R., Duren, R., Hensley, S., Alsdorf, D., 2007. The shuttle radar topography mission. Rev. Geophys. 45 (2). http://dx.doi.org/10.1029/2005RG000183.

Franceschini, A., 1983. Una storia di acque. In: Sitti, R. (Ed.), Vigarano, Storia/Attualità. ArtStudio C, Ferrara, pp. 21–50.

Frizzi, A., 1848. Memorie per la storia di Ferrara. Abram Servadio Editore, Ferrara.

Gahalaut, V.K., Gupta, P.K., Chander, R., Gaur, V.K., 1994. Minimum norm inversion of observed ground elevation changes for slip on the causative fault during the 1905 Kangra earthquake. Proc. Indian Acad. Sci. 103 (3), 401–411.

Goldstein, R.M., Werner, C.L., 1998. Radar interferogram filtering for geophysical applications. Geophys. Res. Lett. 25 (21), 4035–4038. http://dx.doi.org/10.1029/1998GL900033.

Idriss, I.M., Boulanger, R.W., 2008. Soil liquefaction during earthquakes. MNO-12. Earthquake Engineering Research Institute, Oakland, USA (242 pp.).

Ilieva, M., 2011. Crustal deformations of shallow earthquakes in the Eastern Mediterranean studied by radar interferometry and seismology. (Ph.D. thesis), Univ. Paris VI and Bulg. Acad. Sci., Paris (179 pp.).

Iwasaki, T., Tatsuoka, F., Tokia, K.-i, Yasuda, S., 1978. A practical method for assessing soil liquefaction potential based on case studies at various sites in Japan. 2nd Int. Conf. on Microzonation, San Fancisco, Proceedings, pp. 885–896.

Kontoes, C., Elias, P., Sykioti, O., Briole, P., Remy, D., Sachpazi, M., Veis, G., Kotsis, I., 2000. Displacement field and fault modelling for the September 7, 1999 Athens earthquake inferred from Ers-2 Satellite Radar Interferometry. Geophys. Res. Lett. 27 (24), 3989–3992.

Li, Z., Elliott, J.R., Feng, W., Jackson, J.A., Parsons, B.E., Walters, R.J., 2011. The 2010 MW 6.8 Yushu (Qinghai, China) earthquake: constraints provided by InSAR and body wave seismology. J. Geophys. Res. 116, B10302. http://dx.doi.org/10.1029/2011JB008358.

Lin, J., Stein, R.S., 1989. Coseismic folding, earthquake recurrence, and the 1987 source mechanism at Whittier Narrows, Los Angeles basin, California. J. Geophys. Res. 94 (B7), 9614–9632.

M.U.R.S.T. (1997): Carta Geomorfologica della Pianura Padana alla scala 1:250.000. coord. Castiglioni G.B., S.EL.CA., Firenze.

Martelli, L., Molinari, F.C., 2008. Studio geologico finalizzato alla ricerca di potenziali serbatoi geotermici nel sottosuolo del comune di Mirandola. Regione Emilia-Romagna, Servizio Geologico, Sismico e dei Suoli, Bologna.

Massonnet, D., Feigl, K.L., 1998. Radar interferometry and its application to changes in the earth's surface. Rev. Geophys. 36 (4), 441–500. http://dx.doi.org/10.1029/97RG03139.

Massonnet, D., Rossi, M., Carmona, C., Adragna, F., Peltzer, G., Feigl, K., Rabaute, T., 1993. The displacement field of the Landers earthquake mapped by radar interferometry. Nature 364 (6433), 138–142. http://dx.doi.org/10.1038/364138a0.

Meyer, B., Armijo, R., Massonnet, D., de Chabalier, J.B., Delacourt, C., Ruegg, J.C., Achache, J., Papanastassiou, D., 1998. Results from combining tectonic observations and SAR interferometry for the 1995 Grevena earthquake: a summary. J. Geodyn. 26 (2–4), 255–259.

Okada, Y., 1985. Surface deformation due to shear and tensile faults in a half-space. Bull. Seism. Soc. Am. 75, 1135–1154.

Papathanassiou, G., Caputo, R., Rapti-Caputo, D., 2012. Liquefaction phenomena along the palaeo-Reno River caused by the May 20, 2012 Emilia (Northern Italy) earthquake. Ann. Geophys. 55 (4), 735–742. http://dx.doi.org/10.4401/ag-6147.

Pezzo, G., Merryman Boncori, J.P., Tolomei, C., Salvi, S., Atzori, S., Antonioli, A., Trasatti, E., Novali, F., Serpelloni, E., Candela, L., Giuliani, R., 2013. Coseismic deformation and source modeling of the May 2012 Emilia (Northern Italy) earthquakes. Seismol. Res. Lett. 84 (4), 645–655. http://dx.doi.org/10.1785/0220120171.

Pieri, M., Groppi, G., 1981. Subsurface geological structure of the Po Plain, Italy. Consiglio Nazionale delle Ricerche, Progetto finalizzato Geodinamica, sottoprogetto Modello Strutturale, pubbl. N° 414, Roma (13 pp.).

Pizzi, A., Scisciani, V., 2012. The May 2012 Emilia (Italy) earthquakes: preliminary interpretations on the seismogenic source and the origin of the coseismic ground effects. Ann. Geophys. 55 (4), 751–757. http://dx.doi.org/10.4401/ag-6171.

Pondrelli, S., Salimbeni, S., Perfetti, P., Danecek, P., 2012. Quick regional centroid moment tensor solutions for the Emilia 2012 (northern Italy) seismic sequence. Ann. Geophys. 55 (4), 615–621. http://dx.doi.org/10.4401/ag-6146.

Roversi, R., 1989. Assetto idraulico del territorio ferrarese. In: Corbo (Ed.), Terre e acqua.

Salvi, S., Tolomei, C., Merryman Boncori, J.P., Pezzo, G., Atzori, S., Antonioli, A., Trasatti, E., Giuliani, R., Zoffoli, S., Coletta, A., 2012. Activation of the SIGRIS monitoring system for ground deformation mapping during the Emilia 2012 seismic sequence, using COSMO-SkyMed InSAR data. Ann. Geophys. 55 (4), 796–802. http://dx.doi.org/10.4401/ag-6181.

Saraò, A., Peruzza, L., 2012. Fault-plane solutions from moment-tensor inversion and preliminary Coulomb stress analysis for the Emilia Plain. Ann. Geophys. 55 (4), 647–654. http://dx.doi.org/10.4401/ag-6134.

Scognamiglio, L., Margheriti, L., Mele, F.M., Tinti, E., Bono, A., De Gori, P., Lauciani, V., Lucente, F.P., Mandiello, A.G., Marcocci, C., Mazza, S., Pintore, S., Quintiliani, M., 2012. The 2012 Pianura Padana Emiliana seimic sequence: locations, moment tensors and magnitudes. Ann. Geophys. 55 (4), 549–556. http://dx.doi.org/10.4401/ag-6159.

Sonmez, H., 2003. Modification of the liquefaction potential index and liquefaction susceptibility mapping for a liquefaction-prone area (Inegol, Turkey). Environ. Geol. 44 (7), 862–871.

Stein, R.S., King, G.C.P., Rundle, J.B., 1988. The growth of geological structures by repeated earthquakes 2. Field examples of continental dip-slip faults. J. Geophys. Res. 93, 13319–13331.

Wang, C., Shan, X., Wang, C., Ding, X., Zhang, G., Masterlark, T., 2012. Using finite element and Okada models to invert coseismic slip of the 2008 Mw 7.2 Yutian earthquake, China, from InSAR data. J. Seismol. 17 (2), 347–360. http://dx.doi.org/10.1007/s10950-012-9324-5.